Three dimensional shapes of hydrogen-air flames within millimetric Hele Shaw cells

Y. Ballossier, P. Boivin, C. Almarcha

▶ **To cite this version:**

Y. Ballossier, P. Boivin, C. Almarcha. Three dimensional shapes of hydrogen-air flames within millimetric Hele Shaw cells. International Journal of Hydrogen Energy, 2024, 60, pp.333-341. 10.1016/j.ijhydene.2024.02.209 . hal-04591671

HAL Id: hal-04591671
https://hal.science/hal-04591671v1

Submitted on 29 May 2024

HAL is a multi-disciplinary open access archive for the deposit and dissemination of scientific research documents, whether they are published or not. The documents may come from teaching and research institutions in France or abroad, or from public or private research centers.

L'archive ouverte pluridisciplinaire **HAL**, est destinée au dépôt et à la diffusion de documents scientifiques de niveau recherche, publiés ou non, émanant des établissements d'enseignement et de recherche français ou étrangers, des laboratoires publics ou privés.

Three dimensional shapes of hydrogen-air flames within millimetric Hele Shaw cells

Y. Ballossier[a,c,*], P. Boivin[a], C. Almarcha[b]

[a] *Aix Marseille Univ, CNRS UMR7340, Centrale Marseille, M2P2, Marseille, France*
[b] *Aix Marseille Univ, CNRS UMR7342, Centrale Marseille, IRPHE, Marseille, France*
[c] *Institut de Combustion, Aérothermique, Réactivité et Environnement, CNRS-INSIS UPR3021, Orléans, France*

Abstract

Premixed hydrogen-air laminar flames with equivalence ratios ranging from 0.32 to 2.68 adopt different shapes during propagation in a gap (from 1.5 mm to 4.2 mm) between two plates. Thermodiffusive and Darrieus-Landau instabilities are visible for lean mixture while Darrieus-Landau is visible at higher equivalent ratio. Using for the first time simultaneous schlieren visualisation in this configuration, we were able to make two important observations: (i) either symmetric or asymmetric shapes are observed and quantified within the gap as a function of equivalence ratio and gap thickness; (ii) 3D flame surface for unstable laminar flame was estimated. These results validate (or invalidate) the quasi-2D assumptions made in Hele-Shaw cells. Linear stability analysis allowed us to find an *a priori* criteria differentiating symmetric and asymmetric cases. Finally, curvature effect on flame speed enhancement relative to surface amplification is estimated for unstable hydrogen-air laminar flames. This experimental 3D amplification factor provides means to take into account instabilities effect on large scale turbulent models.

Keywords: hydrogen safety; flame instabilities; symmetric / asymmetric flame; Hele-Shaw cell; amplification factor

Introduction

Hydrogen combustion has gained considerable interest in recent years, although experimental and numerical data in the scientific literature are rather scarce compared to hydrocarbon fuels. Indeed, hydrogen flames are barely visible to the naked eye and the thin laminar flame thickness ($\delta_t \sim 0.35$ mm for stoichiometric H_2-air) leads to high computational cost for numerical simulations. However, hydrogen combustion can also generate strong flame acceleration, especially in confined spaces, due to higher laminar flame velocity ($\times 5.7$) compare to CH_4-air mixture at stoichiometry and ambient conditions. Flame surface

*Corresponding author:
Email address: yves.ballossier@cnrs-orleans.fr (Y. Ballossier)

area growth is one of the main parameters driving flame acceleration, as it enlarges the area of heat and mass diffusion transfer between products and reactants, thereby increasing the reaction rate. Flame surface area growth is due to turbulence or intrinsic flame instabilities, usually both [1]. Many turbulent models rely on Damköhler's first hypothesis [2] stating that $S_T/S_L^0 = A_f/A_p$, with S_T the turbulent flame speed, S_L^0 the unstretched laminar flame speed, A_f the flame surface area, and A_p the equivalent planar flame surface. Damköhler's hypothesis gives a good estimation within its validity range [3], but fails for mixtures with non-unity Lewis number and flame with large curvature [4]. The combination of turbulence and thermodiffusive (T-D) instabilities could even generate synergistic interactions [5], i.e. an enhancement of the local variation of the composition compared to laminar cases induced by turbulent fluctuations. Experimental characterization of unstable laminar premixed flame shape and surface area quantification is thus needed to improve numerical models. We aim to facilitate hydrogen combustion studies through a canonical combustor refereed as Hele-Shaw cell [6].

Hele-Shaw cells are used to study flame propagation between two parallel plates separated by a gap several orders of magnitude smaller than the width and height of the plates. A stationary symmetric shape of the flame within the thickness is usually assumed and the problem is considered quasi-2D. Quasi-2D propagation allows to consider the Navier-Stokes equations averaged over the gap [7] reducing momentum equation within the thickness to a relation similar to a Darcy's law [8]. Quasi-2D assumption allows us to derive equations and to compare theoretical and experimental growth rates due to instabilities [9–11]. Simple configurations such as Hele-Shaw cells are also useful to test the sensitivity of thermoacoustic modes to the reactivity of the mixture [12, 13]. However, this configuration can lead to additional vibro-acoustic coupling that can suppress thermoacoustic instabilities [14, 15] or eventually create vibro-acoustic instabilities [16]. From a practical point of view, flame propagation between small gaps is important in the case of accidental leaks in the interstices of fuel cells, for example [17]. This type of configuration is also a model of a micro combustor where gap size has an important effect on thermal and momentum losses [18]. It is important to note that, even very lean hydrogen mixtures could propagate in submillimetre gaps [19–21].

Qualitative evaluation of the flame shape in the Hele-Shaw thickness direction has been performed for hydrocarbons [13, 22], but to date there has been no quantitative experimental characterisation to validate the quasi-2D hypothesis in Hele-Shaw cells for hydrogen flames. Numerical simulations have already highlighted the existence of both symmetric and asymmetric modes [23, 24]. The authors found that heat losses, channel size and inlet velocity of unburned gas affect symmetry map of the flame. In fact, there is a whole range of solutions for the shape of the flame in the thickness [25]. Here, we present an experimental characterisation of the shape of hydrogen-air premixed flames undergoing Darrieus-Landau (D-L) and thermodiffusive (T-D) instabilities in fully optically accessible Hele-Shaw cells that are opened at ignition (top) and closed at the sides and opposite end (bottom). Schlieren diagnostics are performed for simultaneous front and side-view visualization in the Hele-Shaw cell. This configuration allows us to investigate the quasi-2D hypothesis by observing flame shapes between plates under different equivalence ratios and gap sizes. The

equivalence ratio affects flame velocity, sensitivity to D-L, T-D and thermoacoustic (T-A) instabilities [26, 27]. From the simultaneous schlieren visualisation, surface enhancement in front and thickness directions can be quantified to highlight contribution of instabilities and symmetries/asymmetries. This provides insight to correct the flame surface calculated from 2D simulations and account for the consumption speed increase.

Experimental setup

Combustion chambers consist of parallel glass plates (3.3 mm thick) spaced by a distance h of 1.5, 2.3, 2.7, 3.2 or 4.2 mm to form a rectangular parallelepiped of 30 mm width and 150 mm height as shown in Fig. 1. A channel width of 30 mm is chosen to limit the development of a cellular flame structure and to keep the tips of the flame close to the centre of the channel where the side view is focused. Nevertheless, this dimension is large enough to observe the combined effect of D-L and T-D instabilities [28, 29].

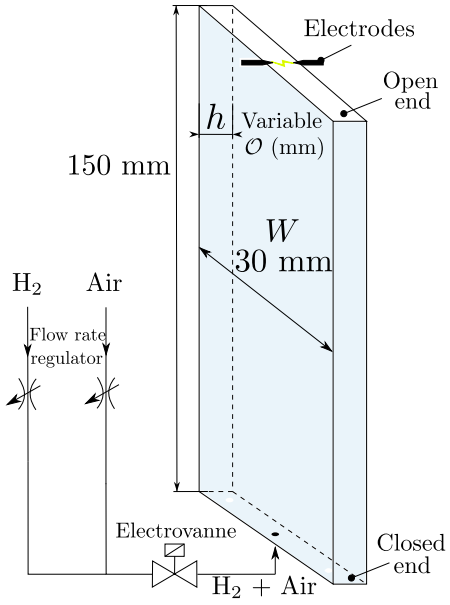

Figure 1: Schematic of Hele-Shaw cell.

For each test, the burner is fed with a pre-mixed reactive mixture from a small hole at the bottom. The upward flow is then stopped and the flame is ignited at the open top end in the same manner: (i) hydrogen and air flow rates are adjusted by mass flow controllers (Bronkhorst EL-Flow select) to achieve the desired equivalence ratio with a precision of $\pm$ 4%. (ii) the ignition sequence is activated, firstly by closing a solenoid valve (PARKER LEGRIS ref. 4202 15 21 20) which cuts off the mixture inlet at the closed end of the chamber; (iii) then, after a fixed delay of 35 ms; the ignition sequence triggers both cameras and activates the electrodes (ignition coil BERU ZSE041 with tungsten electrodes 2 mm in diameter separated by $\sim$ 1 mm, providing about 36 mJ of electrical energy [30]).

The delay between the closing of the solenoid valve and ignition introduces uncertainty into the mixture composition near the open end. However, this delay is necessary to ensure a quiescent flow prior to ignition.

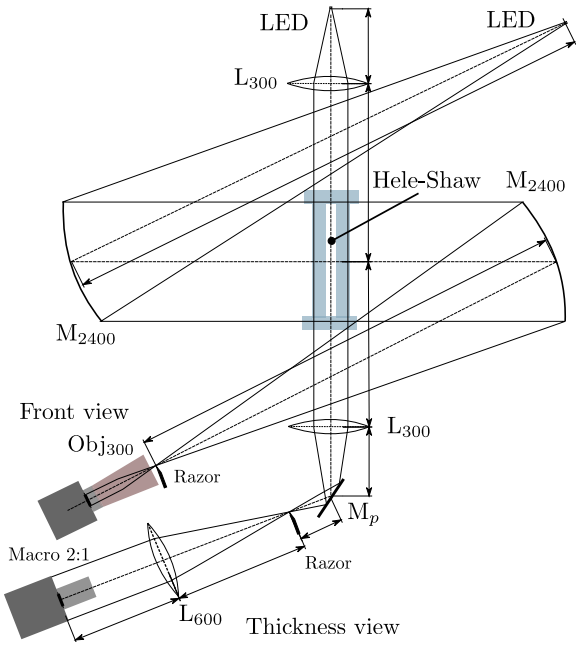

Figure 2: Optical set-up for simultaneous schlieren visualisation in Hele-Shaw cells.

The optical setup used to perform simultaneous visualisation is shown in Fig. 2. The front view LED light source passes through a classic Z-type configuration with two concave mirrors (M_{2400}) and is collected by a 300 mm objective. The thickness view optical path is an in-line lens configuration deflected by a planar mirror (M_p). The collimating and focusing optical pairs have the same focal length (2400 mm for the mirrors and 300 mm for the lens). The collection is realised by a 600 mm focal lens in-line with a 50 mm macro 2:1 lens. The light is filtered by horizontal razor blades that are oriented towards the direction of burned gases in order to brighten the flame front. For the thickness view, the blade is located at the focal length of L_{300} and L_{600} to provide an image magnification of $\times 2$, resulting in a total image magnification of $\times 4$ with the macro lens. In the Z-type configuration, a 3W white LED (0.8×1.5 mm^2) is used as the light source, but to ensure adequate illumination within the thickness, a 10 W green LED (1.2×1.2 mm^2) is used instead. Both cameras are Photron Fast Cam MiniAX with a maximum resolution of 1Mpixel, operated at 10 kHz and 0.1 ms exposure time. This method allows a resolution of 160 μm/pixel and 5 μm/pixel for the front and thickness view respectively.

In terms of post-processing, the images are blurred after background subtraction, then binarised using Otsu thresholding [31] to detect the flame front. Consumption speed is measured from linear interpolation ($R^2 > 0.95$) of the area of burned gas as a function of time in the front direction divided by the channel width. All images are colour inverted to show areas where light is deflected by the flame in black.

Results & Discussion

Initial propagation and development of instabilities - front view

Upon ignition with the electrodes in the centre (on the upper edge side), the flame propagates towards the closed end confined between the two plates. The flame surface grows smoothly due to mass and thermal diffusion. As the circular flame propagates, the curvature decreases as the flame radius increases, and consequently the spatial flame velocity increases or decreases, depending on the flame response to stretch and curvature, referred to as the Marsktein length $\mathcal{L}$ [32–35].

This mechanism drives the initial smooth phase in our Hele-Shaw cells, which is also affected by heat and momentum losses, while the expansion of burned products has little effect because the open end on the ignition side suppresses the piston effect.

The density jump across the flame, causes a deviation of the non-perpendicular unburned streamlines and acceleration of the flow passing through the flame, in accordance with the conservation of mass [36]. Smooth flame propagation ends due to instabilities that develop and corrugates the flame at a critical distance from ignition. This distance, called R_{crit} for spherical flames, is associated with the critical Peclet number $Pe_c = R_{crit}/\delta_\nabla$ where $\delta_\nabla = (T_b - T_u)/\max(\nabla T)$ is the flame thickness. In other words, instabilities are triggered when advection overcomes thermal diffusion. It is known that the critical radius of freely propagating spherical H_2-air flames decreases with increasing pressure and increases with the equivalent ratio [33, 37]. The presence of walls decreases R_{crit} significantly (between 8 and 22 mm at $\phi = 1$ compared to free spherical flames [38] $R_{crit} \sim 75$ mm [39] for H_2-air at $\phi = 1$). Indeed, the sensitivity to perturbations induce a large deviation in the measured R_{crit} and lead to earlier development of instabilities in confined spaces.

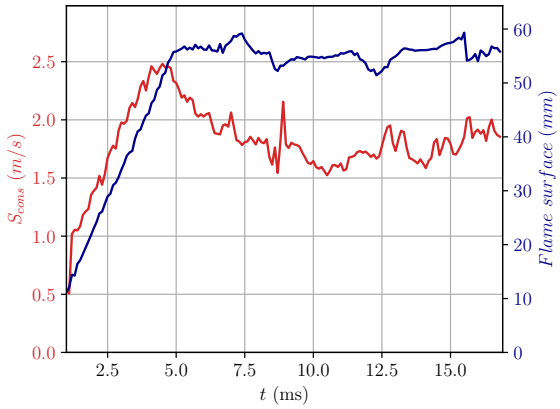

Figure 3: Consumption rate (red) with flame surface (blue) as a function of time. Front view of the H_2-air flame at ambient conditions (ϕ=0.57).

However, despite the development of instabilities, a steady consumption rate S_{cons} (defined as the rate of increase of the burned gas area divided by channel width) is observed with small fluctuations due to cell splitting and cell merging (see Fig.3). Splitting of the crest (the leading part of the flame) decreases the front burning rate, while merging of the cusps

increases it [40]. Non-accelerating flames within Hele-Shaw was also reported for smaller gap size (0.4 mm), with lean H_2-O_2 [20] and in larger gap (12.7 mm) for H_2-air mixture [8, 41]. While unstable flames significantly increase the flame area, the consumption rate in our Hele-Shaw cells saturates to a quasi-steady value far from the opposite wall where a closed boundary could affect the flame.

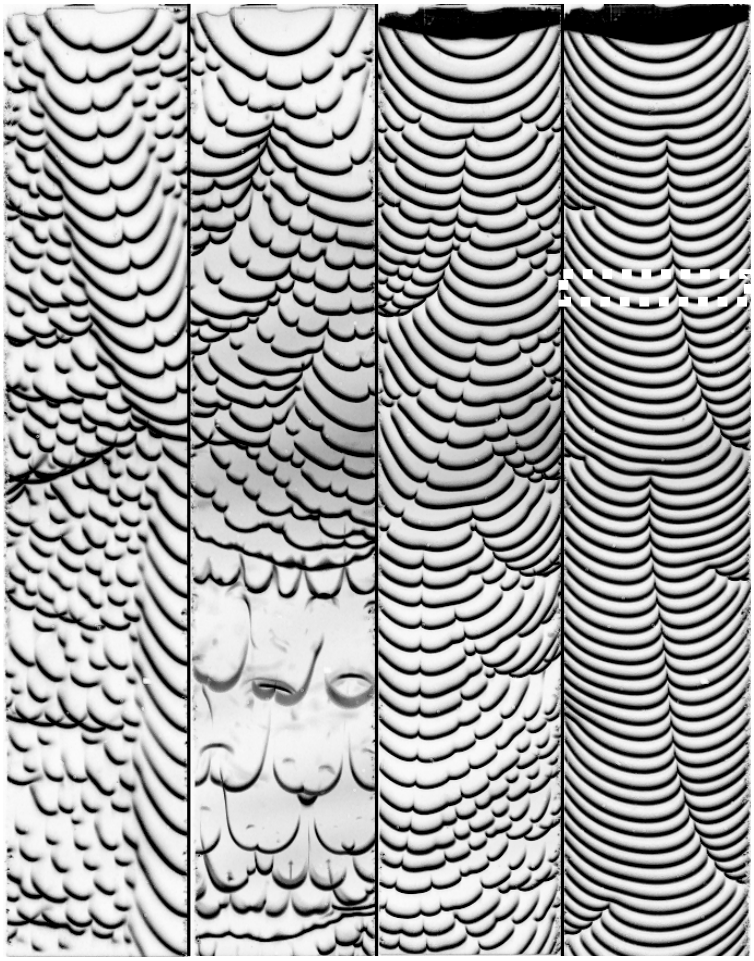

Figure 4: Chronophotography of H_2-air instabilities at ambient conditions. Hele-Shaw cell of 3.2 mm thickness, visualization window: 25×138 mm. From left to right: $\phi = 0.32$ with characteristic pattern of T-D instabilities ($\Delta t = 10$ms); $\phi = 0.40$ with T-A instabilities at the end of the chamber ($\Delta t = 5$ms); $\phi = 0.78$ ($\Delta t = 1$ms); ; $\phi = 1.48$ with D-L instabilities ($\Delta t = 0.5$ms). White dotted box indicate the window of simultaneous schlieren visualisation.

Figure 4 illustrates the manifestation of characteristic instabilities in the Hele-Shaw cell as the equivalence ratio (ϕ) increases from left to right. If the effective Lewis number (Le^{eff}) [42] is small enough (below Le_{critical}), as it is the case for the lean H_2-air mixture ($\phi = 0.32$) shown in Fig. 4 left, a characteristic T–D finger-like structure with local extinction of the mixture in concave regions [43, 44] is visible.

As the equivalence ratio increases ($\phi = 0.40$) in the second image from the left on Fig. 4 finger-like structures are still present. In the centre of the channel, T-A flattens the flame

front before inducing strong oscillations as described in [12, 16, 45]. The amplitude of these oscillations decreases as the flame reaches the end of the duct. Increasing the H_2 fraction ($\phi = 0.78$) produces wider cells visible in the first half of the channel before smaller cells appear in the lower right part. The cells on the left propagate faster and induce an upward movement of the unburned mixture on the right side of the chamber [46]. Finally, in the right image of Fig. 4 only large scale cells associated with D-L instability are visible for large equivalence ratio ($\phi = 1.48$). In this 30 mm wide channel these large scale D-L cells almost disappear for $\phi = 2.68$. Linear analysis of D–L instabilities [26, 47, 48] showed that perturbation of small wavelength, λ, leads to unconditional stabilisation of D–L cells below a critical value λ_c. Since λ_c increases with the equivalence ratio for rich mixtures, fewer cells are visible on the right hand side of Fig. 4.

The behavior shown in Fig. 4 should not change when the flame propagates from bottom to top. Buoyancy forces do not significantly alter the maximum pressure for $\phi \geq 0.32$ as demonstrated experimentally within Hele-Shaw cells of larger gap size ($h = 10$ mm) by Veiga-López et al. [45]. For leaner mixtures, upward propagating flames have larger perturbation wavelengths compared to downward propagating flames [45].

Asymmetry map - thickness view

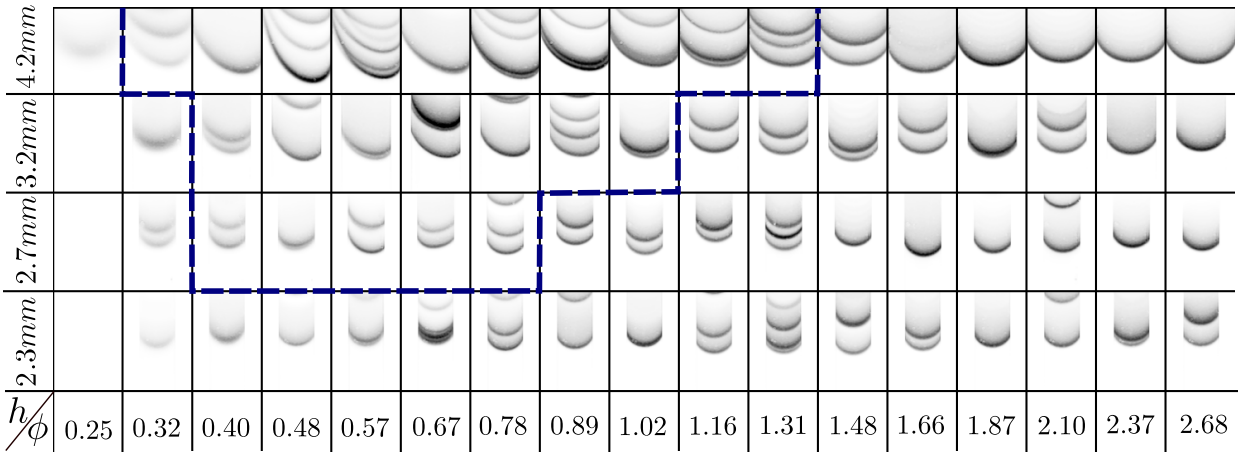

Figure 5: Flame shapes in Hele-Shaw cells with a variable gap. H_2-Air at ambient conditions. Raw inverted schlieren images.

Flame propagation is now observed between the plates of the Hele-Shaw cells to describe flame shape in this direction. Schlieren diagnosis is performed on the upper part of the chamber to avoid the appearance of T-A instabilities and far enough from ignition to avoid transient effects. The visualisation window is located about 40 mm from the ignition and corresponds to the dotted white box in Fig. 4 right. The flame consumption speed remains quasi-steady in this region, as described in the previous subsection. Depending on the gap size, h, between the plates and equivalence ratio, ϕ, of the mixture, symmetric or asymmetric flame shapes are generated within the thickness as shown in Fig. 5 (separated by the blue dotted line). Observed flames are always curved between plates. Several flame fronts are

sometimes visible on Fig. 5. This is due to the integrated information collected by the schlieren diagnostic, which shows different cell tips visible in the front direction (Fig. 4). Note that all fronts do not move at the same speed due to flame-induced perturbations of the flow ahead of the flame. Finally, some cells may be advected upwards. When those cells are symmetric, they all have the same shape, but asymmetric cases exhibit different shapes and different cell tips, especially visible in Fig. 5 for $h = 4.2$ mm and $\phi = 0.48$ and 0.57. This is evidence of flame shape heterogeneity for asymmetric cases, while for symmetric cases the flame maintains a constant shape, an important assumption for 2D simulations. In the present results and discussion sections we focus on the lower front (closest to the ground) which has the maximum downward velocity. The flame shape for smaller gap size (1.5 mm not shown here) was symmetric for all equivalence ratios tested. The range of equivalent ratio with asymmetric shapes increases as the gap size is increased up to $\phi = 1.31$ for $h = 4.2$ mm. On the lean mixture side, transition from symmetric to asymmetric is sharper as a function of gap size between $h = 3.2$ mm and $h = 4.2$ mm for $\phi = 0.32$. Below $\phi = 0.25$ and $h = 4.2$ mm the flame did not propagate far enough within the thickness to reach the visualisation window. Observations made at different distances from ignition showed no significant changes in flame shape compared to Fig.5, except in the case of T-A instabilities.

The asymmetry factor (S) is calculated as, $S = \frac{2}{hr_f}(|A_a - A_b|)$, where A_a and A_b are the surface area of the flame on each side of the half-gap distance (noted a and b on Fig. 6), $h/2$ is the half-gap distance, and r_f is the flame extension (distance between the tip and the tail). This method provides an asymmetry factor between 0 (if the flame is perfectly symmetric) and 1 (if the flame is completely asymmetric). This normalisation also makes it possible to compare different gap distances and flame lengths. An equivalent method is used to define the asymmetry factor in [23, 24]. The difference between our definition and that of Jiménez et al. [24] is only a factor of 2. As a result, the symmetry factor in our case is limited to values strictly between 0 and 1.

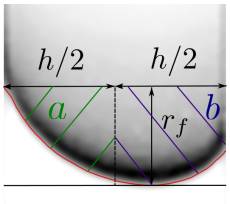

Figure 6: Illustration of the front detection algorithm (red line) along with the method used to define asymmetry factor.

Figure 7 shows the quantification of the asymmetry factor in our configuration. Detection failures close to the wall causes high scattering between tests and are filtered out to keep the centre of the flame. The maximum value of S is reached for $\phi = 0.57, 0.67$ and 0.48 for $h = 2.7$ mm, 3.2 mm and 4.2 mm respectively. An asymmetric factor threshold of 0.15 is chosen to distinguish symmetric (filled symbols) from asymmetric (empty symbols) cases for the remainder of the discussion.

In order to apply quasi-2D hypothesis in theoretical and numerical simulations we need to know *a priori* whether the flame is rather symmetrical or not. Indeed, asymmetric

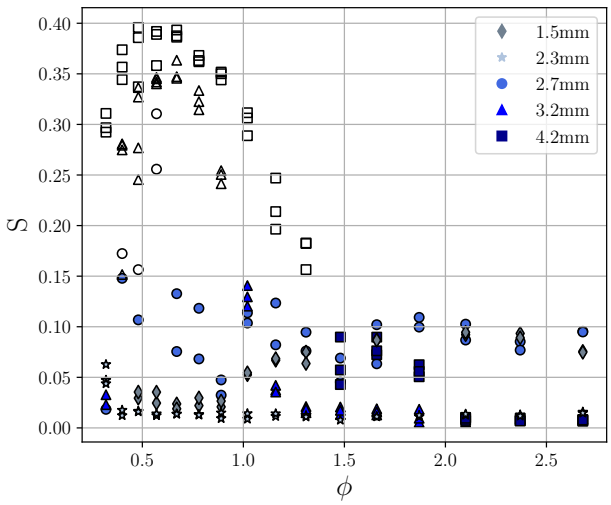

Figure 7: Asymmetry factor as a function of equivalence ratio calculated with the method displayed on Fig;6. H_2-air at ambient conditions. Empty symbols represent cases with $S > 0.15$.

cases showed a heterogeneous front structure along the width of the channel, leading to heterogeneity of the flow. First along the width, but also within the thickness, making the application of Darcy's law or the assumption of Poiseuille flow further away from reality compared to a symmetric case.

Criteria for asymmetric/symmetric distinction

A first criterion to distinguish symmetric from asymmetric cases was proposed in [23] as the ratio of gap size to flame thickness h/δ_∇. The authors numerically observed that below a critical value only symmetric cases are stable. This result has been confirmed by several numerical studies [24, 40]. However, while there is a critical gap distance below which only symmetric cases exist (see Fig. 5), symmetry is still present for $h/\delta_\nabla \sim 12$ as shown in Fig. 8 (a). In addition, sensitivity of δ_∇ calculations for lean mixtures induce variability of the critical value. This motivates the need to find another criterion for the prediction of asymmetric/symmetric flames. Note that consumption speed for lean mixtures and small gap size (up to $\sim 5 \times S_L^0$ on Fig. 8 (a)) emphasises the risk related to the enhancement of the destabilising effect of T-D with the increase in heat losses [49]. Those measurement also confirms numerical results of the T-D induced velocity increase obtained in [29] ($\sim 4-5 \times S_L^0$ for sufficiently large lateral 2D domains).

The linear stability analysis of the flame front gives us the growth rate associated with the wave number of the perturbation, known as the dispersion relation (Eq. 1 obtained from [26] neglecting higher order terms and with B_1, B_2 and B_3 coefficients for variable transport).

$$\omega = \omega_{dl} S_L^0 k - \delta_\nabla [B_1 + \beta(Le^{eff} - 1)B_2 + PrB_3] S_L^0 k^2 \tag{1}$$

In Eq.1 ω is the growth rate, β the Zeldovich number, Pr the Prandtl number, k the

wavenumber of the perturbation, and $\sigma = \rho_u/\rho_b$ the ratio of unburnt to burnt density, ρ_u and ρ_b respectively. Finally, Le^{eff} is the effective Lewis number defined as [42]:

$$Le^{eff} = \begin{cases} Le^{deficient} = Le^{H_2}, \text{ for } \phi < 0.6 \\ \frac{Le^{excess} + ALe^{deficient}}{1+A}, \text{ with } \begin{array}{l} A = 1 + \beta(1/\phi - 1), \text{ for } 0.6 < \phi \leq 1 \\ A = 1 + \beta(\phi - 1), \text{ for } 1 \leq \phi < 1.4 \end{array} \\ Le^{deficient} = Le^{O_2}, \text{ for } 1.4 < \phi \end{cases} \tag{2}$$

where Le^{H_2} and Le^{O_2} are the ratios of the thermal and molecular diffusivity of hydrogen and oxygen, respectively. Following Eq. 1, identical as Matalon [26], the condition

$$\omega(k_c) = 0 \tag{3}$$

leads to

$$k_c = \frac{\omega_{dl}}{\delta_\nabla [B_1 + \beta(Le^{eff} - 1)B_2 + PrB_3]} \tag{4}$$

with,

$$\omega_{dl} = \frac{1}{\sigma + 1}[\sqrt{\sigma^3 + \sigma^2} - \sigma] \tag{5}$$

From Eq. 4, obtained for Lewis number close to unity, we can calculate the cut-off wavelength ($\lambda_c = 1/k_c$) below which the flame is stable (i.e. $\omega < 0$). The flame properties used, given in Table 1, are calculated with Cantera [50] using the Mével [51, 52] mechanism and the Shock and Detonation Toolbox [53]. Matalon and Bechtold developed Eq. 1 for the inviscid case of unconfined flames, which is far from our experimental conditions. However, Eq. 1 provides a straightforward method for calculating the growth rate as a function of wavenumber, which gives an estimate of λ_c. Nevertheless, an accurate determination of λ_c requires a detailed numerical investigation [44, 54].

Results presented on Fig. 8 (b) show that for $h/\lambda_c < 0.85$ all cases are symmetric. If the gap size is less than λ_c, all perturbations will be dumped. In this case no perturbation can grow, as they are necessarily smaller than λ_c due to geometric confinement. Here, with a gap size above 85% of the calculated λ_c, asymmetric flames can form. Numerical study [27] showed that for channel gaps above λ_c the asymmetric flame is always the viable solution. Two conclusions can be drawn from these observations: (i) either the dumping process of perturbations with wavelength $0.85\lambda_c < \lambda < \lambda_c$ could form an asymmetric shape, or; (ii) the calculation from Eq. 1 overpredicts λ_c and only perturbations with $\lambda > \lambda_c$ grow to form an asymmetric flame.

In fact, Eq. 1 is outside its validity limits for lean H_2-air mixtures because the thin flame approximation is not applicable anymore (from $\delta_\nabla = 0.66$mm for $\phi = 0.4$ to $\delta_\nabla = 1.68$mm for $\phi = 0.32$). On the other hand, for lean mixtures, different kinetic mechanism could lead to large variations ($> 20\%$) of δ_∇ and are certainly over-predicted with 1D flame calculations. More detailed numerical simulations considering T-D instabilities showed larger k_c for lean H_2 mixtures ($k_c \sim 2.1\delta_\nabla$ for $\phi = 0.4$) [44, 54]. The authors in [44, 54] observed

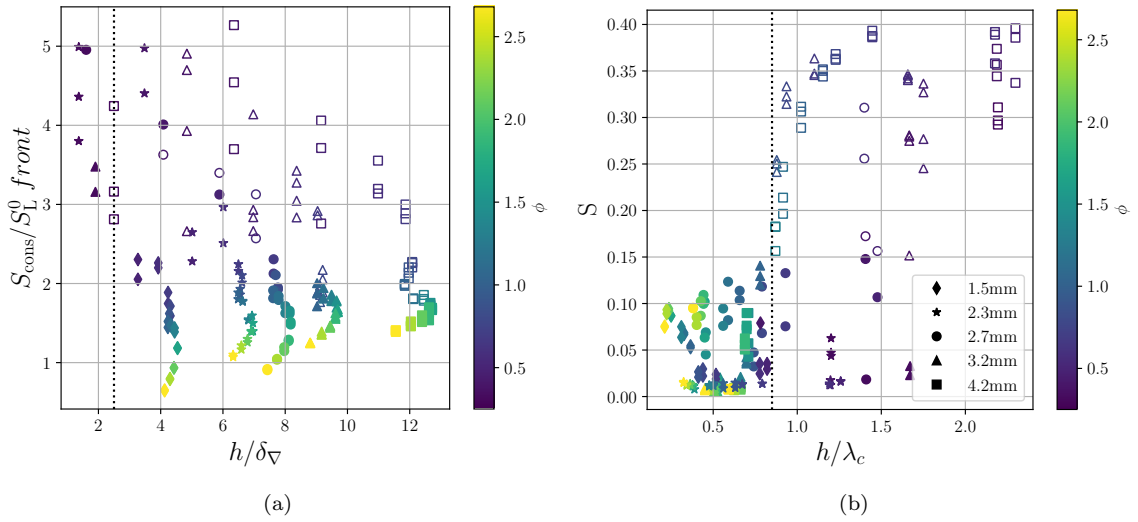

Figure 8: Left: Consumption speed S_{cons} (front direction) nondimensionalised by unstretched laminar flame speed S_L^0 as a function of gap size, h, adimensioned by flame thickness, δ_∇. Right: Asymmetry factor as a function of channel gap (h) adimensioned by theoretical cut-off wavelength (λ_c). Empty symbols represent asymmetric cases. Black dotted lines indicate the criteria below which only symmetric flame exist.

an augmentation of λ_c for mixtures with $\phi < 0.5$, not captured with the model of Eq. 1. This augmentation would increase the ratio h/λ_c, improve the correlation on Fig. 8 of leaner mixtures, and increase the critical value above which asymmetric flames exist. The dependence of the flame properties on the k_c calculation from Eq. 4 is also important. In Tab. 1 Zeldovi'ch number (β) is calculated from the explosion theory [56] and the flame thickness from the temperature gradient. Nevertheless, this criterion retains the advantages of being easily computable and giving accurate predictions to distinguish asymmetric from symmetric cases for mixtures where $\phi \sim 1$. Although, extension to lean mixtures require more detailed determination of λ_c.

Flame surface and influence on velocity

Interplay between surface growth and flame velocity needs to be accounted in 2D numerical and theoretical studies to model 3D effects. Via a source term to account for the extra surface and acceleration induced for example. Figure 9 shows the mean consumption speed in the front view within the simultaneous visualisation window (front and thickness). The overall evolution follows the same trend as the unstretched laminar flame speed (black line), with some variations due to the gap size. The trends observed in Fig. 5 and Fig. 9 should remain the same with a different heat flux. However, the minimum gap size below which volumetric heat release becomes small relative to surface heat losses, will be affected. For instance, there is no observable impact of gap size on consumption speed between $h = 3.2$ and 4.2 mm, while the asymmetry map is affected. Assuming identical convective heat exchange coefficients for all gap sizes, the heat losses at the walls are equal for the same composition. In the case of a smaller gap, as the heat losses are almost constant, only the

Table 1: Combustion properties of the H_2-Air mixtures studied. Initial conditions: $p_0 = 100$ kPa, $T_0 = 300$ K.

ϕ	δ_∇ (mm)	S_L^0 (m/s)	σ	β	Le^{eff}	Pr	B1	B2	B3	λ_c (mm)
0.32	1.68	0.11[1]	3.9	5.4	0.31	0.69	7.75	2.15	1.95	1.91
0.4	0.66	0.2	4.44	4.77	0.31	0.68	9.36	2.46	2.59	1.92
0.48	0.46	0.41	4.92	4.51	0.31	0.68	10.89	2.74	3.21	1.82
0.57	0.38	0.69	5.4	4.26	0.32	0.68	12.5	3.02	3.89	1.93
0.67	0.35	1.03	5.87	3.92	0.53	0.68	14.12	3.29	4.59	2.9
0.78	0.35	1.39	6.31	3.55	0.6	0.67	15.67	3.55	5.27	3.42
0.89	0.35	1.73	6.66	4.12	0.67	0.67	16.93	3.75	5.84	3.64
1.02	0.35	2.07	6.9	4.9	0.8	0.66	17.83	3.89	6.25	4.11
1.16	0.35	2.36	6.87	4.74	0.94	0.63	17.74	3.87	6.21	4.59
1.31	0.34	2.59	6.74	4.61	1.06	0.6	17.24	3.79	5.98	4.83
1.48	0.33	2.75	6.58	4.67	1.39	0.58	16.64	3.7	5.71	5.92
1.66	0.33	2.83	6.41	4.63	1.46	0.56	16.02	3.6	5.43	6.01
1.87	0.33	2.83	6.22	4.46	1.52	0.54	15.34	3.49	5.13	6.1
2.1	0.34	2.76	6.02	4.51	1.58	0.52	14.64	3.38	4.82	6.34
2.37	0.35	2.64	5.81	4.7	1.64	0.51	13.89	3.26	4.49	6.72
2.68	0.36	2.46	5.58	4.7	1.69	0.5	13.11	3.12	4.15	7.1

[1] Interpolated from experimental data [55].

heat release decreases due to smaller amounts of reactive within the plates, thus reducing the consumption rate.

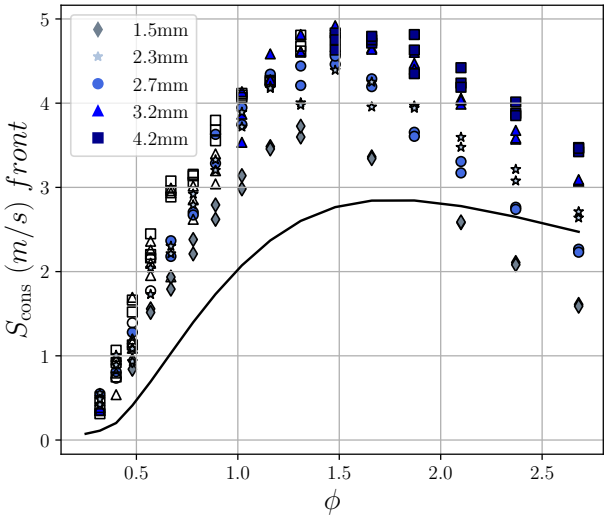

Figure 9: Mean consumption speed, S_{cons} (increase rate of burned gas area), measured from front direction, along with a black line indicating unstretched laminar flame speed, S_L^0. Empty symbols represent asymmetric case. H_2-Air at ambient conditions.

From the flame front, we can calculate the sum of the Euclidean distances between pixels to obtain the flame area. The median value is calculated over the time interval that corresponds to the common viewing range for both views. Flame area is measured separately from front and thickness directions and adimensioned by the Hele Shaw horizontal extension and gap width respectively, to obtain the 2D wrinkling factor, Ξ_{2D}, on Fig. 10 (A_{front}/W and A_{thick}/h for front (blue) and thickness (red) direction respectively). Both Ξ_{2D} show an increase in area relative to flat flame, especially for lean mixtures. Wrinkling factor remains higher in the thickness than in the front direction for rich mixture. The opposite trend is observed for lean mixtures. Cases with asymmetries (empty symbols) exhibit higher dispersion. The differentiation between the symmetric and asymmetric cases is more apparent for A_{thick}/h. For rich mixtures ($\phi > 1$), confinement moderates A_{thick}/h. Indeed, for $\phi = 2.68$ the surface increases by 14% compared to the planar flame for $h =$ 1.5mm, but goes up to 26% for h=4.2mm. From the front direction, confinement starts to play a role for $\phi > 1.5$ with area variation of 10%. Cell dynamics remains the main mechanism driving the increase in flame area and consumption speed in the front direction.

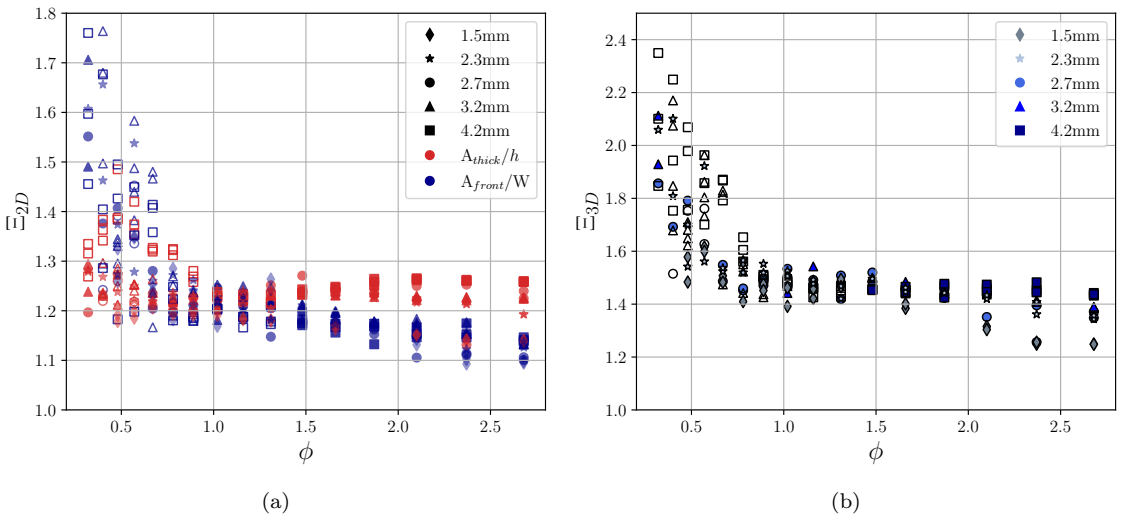

Figure 10: (a) 2D winkling factor computed from flames area, A_{front} and A_{thick}, adimensioned by channel width (W) and by gap size (h), for front (blue) and thickness (red) direction respectively, as a function of equivalent ratio. (b) 3D wrinkling factor, $\Xi_{3D} = (A_{thick}/h) \times (A_{front}/W)$. H_2-air at ambient conditions.

Asymmetric flames increase flame area up to almost 50% compared to flat flames ($\sim$ 25% for symmetric flames). However, the maximum increase in flame area is due to T-D instabilities at $\phi = 0.32$ with an increase close to 176% probably due to larger heat losses effect amplifying T-D instabilities for low Le^{eff} [49, 57]. Note that for $\phi = 0.32$ and $h = 2.3$mm, lateral confinement along the width induces an inverted T-D corrugated V-shape flame in the front view, resulting in a larger surface increase of 240% compared to a flat flame (cropped on Fig. 10 for clarity).

Two-dimensional theoretical analysis by Yanez et al. [58] based on the Sivashinsky equation showed that the mean wrinkling factor is around 1.4 (40% surface increase with a

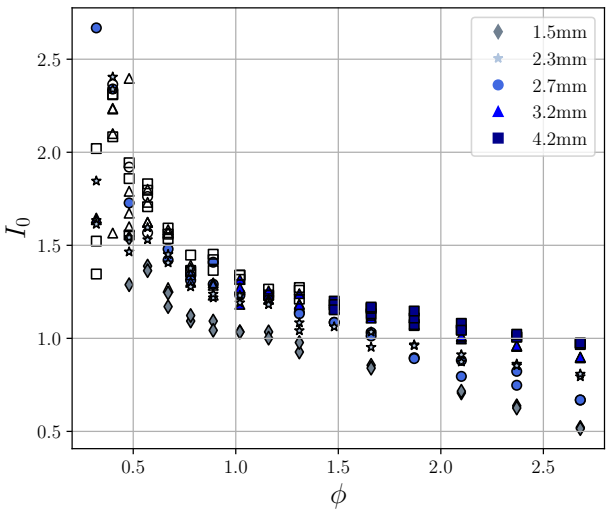

Figure 11: Amplification factor, $I_0 = (\mathrm{S}_{cons}/\mathrm{S}_L^0)/(\Xi_{3D})$, with $\Xi_{3D} = (A_{thick}/h) \times (A_{front}/W)$ as a function of equivalent ratio ϕ and gap size h. H_2-Air at ambient conditions.

maximum of 52% for $\phi = 0.85$). Measurements in the front direction show a higher wrinkling factor for lean mixtures due to T-D instabilities, but a lower one for D-L alone. In our cases, the 3D wrinkling factor, $\Xi_{3D} = A_f/A_p = (A_{thick}/h) \times (A_{front}/W)$ displayed on Fig. 10 (b), reaches a constant value around 1.5 for rich mixture if the gap size is large enough (when the heat losses do not significantly affect the flame). Although a value up to 2.3 is reached for lean mixtures. This calculation of Ξ_{3D} assumes that the flame shape remains constant along the entire channel width. As mentioned earlier, consideration of a constant shape along the width is a strong assumption for asymmetric cases, but seems to be valid for symmetric cases (see Fig. 5). Reconstruction of Ξ_{3D} from 2D measurements made on freely spherical flames leads to similar values for lean H_2-air mixture [59].

To take into account the effect of flame surface wrinkling on flame velocity enhancement Fig. 11 displays the amplification factor, defined in [29] as, $I_0 = (S_{cons}/S_L^0)/(\Xi_{3D})$, as a function of equivalent ratio. In fact, for a negative burnt Markstein length (lean side), $\mathrm{S}_{cons}/\mathrm{S}_L^0$ is greater than Ξ_{3D} ($I_0 > 1$). Close to $\mathcal{L}_b = 0$ (stoichiometry) I_0 remains positive ($1 < I_0 < 1.5$), before decreasing as $\mathcal{L}_b$ increases (rich side). A faster decrease is observed for smaller gap sizes, probably due to larger heat losses compare to volumetric heat production. Increasing the surface area of the corrugated flame leads to greater curvature of the flame front, providing additional velocity enhancement for negative $\mathcal{L}_b$, whereas positive $\mathcal{L}_b$ mitigates this feedback. Similar results were obtained in 2D numerically [29, 44] and experimentally by 2D tomography on spherical flames [60], and are confirmed here with 3D measurements. Presence of T-D instabilities also induce local variations of the equivalence ratio [5, 44], leading to local variations of the laminar flame speed, which could cause an overestimation of the local amplification factor. Note that unstretched laminar flames speed are computed from 1D flame (displayed on table 1) and provide a lower value than experi-

mental determination, especially for lean mixture [38, 61, 62]. An experimental value is thus used for the leanest mixture studied ($\phi = 0.32$). Figure 11 demonstrate that Damköhler's first hypothesis cannot be applied for mixtures with negative $\mathcal{L}_b$, and turbulent model used for hydrocarbons need to account for instabilities induced amplification factor.

Conclusion & Perspectives

A first experimental quantification of the asymmetry factor is presented in Hele-Shaw cells with different thicknesses and for several equivalence ratios. Flame fronts are always curved between plates. Either symmetric or asymmetric flame shapes are observed depending on ϕ, with an increasing range of asymmetric cases as the gap size increases. The homogeneity of the symmetrical flame shape brings the quasi-2D assumption closer to reality, while the heterogeneity of the asymmetrical flame shape requires more precautions.

Our experimental results confirm numerical studies stating that below a certain gap only a symmetric shape exists. Another criterion based on Matalon and Bechtold's dispersion relation, h/λ_c seems more appropriate than flame thickness to distinguish symmetric from asymmetric cases. Actually, asymmetric shapes appear to exist between plates only when the channel gap is at least of the order of cut-off wavelength. To confirm this trend, a better determination of λ_c for lean mixtures is required.

As D-L dominates for rich mixtures, the velocity deficit increases with confinement for smaller gaps. For lean mixtures, no significant effect of gap size on velocity is observed, probably due to competition between D-L and T-D. However, presence of asymmetry affect significantly the consumption speed.

The combination of simultaneous schlieren visualisation allows us to estimate the total flame area. Symmetric and asymmetric flames lead to an increase in flame area of 25% and 50%, respectively, compared to planar flames. While asymmetric cases increase the flame area, the contribution of instabilities within the front direction remains larger for lean mixtures (ϕ <0.5). Curvature within the thickness generates more wrinkling than in the front direction only for rich mixtures. Estimation of the 3D wrinkling factor showed that for $\phi > 1$, the overall flame surface is 50% larger than the channel cross section if channel gap is large enough (less otherwise). For lean mixture this value can reach up to 230%.

The evolution of the flame velocity compared to the unstretched laminar velocity as a function of the 3D wrinkling factor gives us a first experimental amplification factor. Negative Markstein mixtures are capable of greater velocity enhancement than area increase alone, due to flame response to stretch and curvature generated by the instabilities. To the authors' knowledge, this is the first experimental quantification of this known effect taking into account the 3D flame surface effect on premixed flame propagation velocity. This first experimental estimation of the amplification factor allowed to quantify effect of surface enhancement on laminar flames, and will hopefully contribute to the development of a model capable to handle turbulence and instabilities for lean hydrogen air mixtures. As a matter of fact, amplification factor measurement confirm that Damköhler's first hypothesis is not applicable for lean H_2-air mixtures.

Finally, influence of the calculation method of the flame properties should be considered in detail. Unburned gas flow in front of the flame as well as heat losses at the walls must be taken into account in order to assess the influence of heat and momentum losses on flame shapes within the thickness and instabilities. Indeed, effect of losses on amplification factor is not negligible.

Acknowledgments

This research was supported by IMI Institut Mécanique et Ingénierie funding and the ECOSAFE ANR project ANR-21-CE05-0028.

References

[1] S. Yang, A. Saha, Z. Liu, C. K. Law, Role of Darrieus–Landau instability in propagation of expanding turbulent flames, Journal of Fluid Mechanics 850 (2018) 784–802. doi:https://doi.org/10.1017/jfm.2018.426.

[2] T. Poinsot, D. Veynante, Theoretical and Numerical Combustion, Edwards, 2005.

[3] M. Klein, A. Herbert, H. Kosaka, B. Böhm, A. Dreizler, N. Chakraborty, V. Papapostolou, H. G. Im, J. Hasslberger, Evaluation of flame area based on detailed chemistry DNS of premixed turbulent hydrogen-air flames in different regimes of combustion, Flow, Turbulence and Combustion 104 (2020) 403–419. doi:https://doi.org/10.1007/s10494-019-00068-2.

[4] N. Chakraborty, D. Alwazzan, M. Klein, R. S. Cant, On the validity of Damköhler's first hypothesis in turbulent bunsen burner flames: A computational analysis, Proceedings of the Combustion Institute 37 (2) (2019) 2231–2239. doi:https://doi.org/10.1016/j.proci.2018.07.042.

[5] L. Berger, A. Attili, H. Pitsch, Synergistic interactions of thermodiffusive instabilities and turbulence in lean hydrogen flames, Combustion and Flame 244 (2022) 112254. doi:https://doi.org/10.1016/j.combustflame.2022.112254.

[6] J. Sharif, M. Abid, P. Ronney, Premixed-gas flame propagation in hele-shaw cells, in: Joint US Sections Combustion Institute Meeting, 1999.
URL https://ntrs.nasa.gov/citations/20000005014

[7] G. Joulin, G. Sivashinsky, Influence of momentum and heat losses on the large-scale stability of quasi-2D premixed flames, Combustion Science and Technology 98 (1-3) (1994) 11–23. doi:https://doi.org/10.1080/00102209408935393.

[8] D. Fernández-Galisteo, V. N. Kurdyumov, P. D. Ronney, Analysis of premixed flame propagation between two closely-spaced parallel plates, Combustion and Flame 190 (2018) 133–145. doi:https://doi.org/10.1016/j.combustflame.2017.11.022.

[9] E. Al Sarraf, C. Almarcha, J. Quinard, B. Radisson, B. Denet, P. Garcia-Ybarra, Darrieus–Landau instability and Markstein numbers of premixed flames in a hele-shaw cell, Proceedings of the Combustion Institute 37 (2) (2019) 1783–1789. doi:https://doi.org/10.1016/j.proci.2018.05.030.

[10] B. Radisson, B. Denet, C. Almarcha, Nonlinear dynamics of premixed flames: from deterministic stages to stochastic influence, Journal of Fluid Mechanics 903 (2020). doi:https://doi.org/10.1017/jfm.2020.562.

[11] M. Tayyab, B. Radisson, C. Almarcha, B. Denet, P. Boivin, Experimental and numerical lattice-boltzmann investigation of the Darrieus–Landau instability, Combustion and Flame 221 (2020) 103–109. doi:https://doi.org/10.1016/j.combustflame.2020.07.030.

[12] G. Searby, Acoustic instability in premixed flames, Combustion science and technology 81 (4-6) (1992) 221–231. doi:https://doi.org/10.1080/00102209208951803.

[13] F. Veiga-López, D. Martínez-Ruiz, E. Fernández-Tarrazo, M. Sánchez-Sanz, Experimental analysis of oscillatory premixed flames in a hele-shaw cell propagating towards a closed end, Combustion and Flame 201 (2019) 1–11. doi:https://doi.org/10.1016/j.combustflame.2018.12.005.

[14] G. Searby, D. Rochwerger, A parametric acoustic instability in premixed flames, Journal of Fluid Mechanics 231 (1991) 529–543. doi:10.1017/S002211209100349X.
[15] M. Rubio-Rubio, F. Veiga-López, D. Martínez-Ruiz, E. Fernández-Tarrazo, M. Sánchez-Sanz, Suppression of thermoacoustic instabilities by flame-structure interaction, Proceedings of the Combustion Institute 39 (2) (2023) 1577–1585. doi:https://doi.org/10.1016/j.proci.2022.07.165.
[16] B. Radisson, J. Piketty-Moine, C. Almarcha, Coupling of vibro-acoustic waves with premixed flame, Physical Review Fluids 4 (12) (2019) 121201. doi:https://doi.org/10.1103/PhysRevFluids.4.121201.
[17] M. Kuznetsov, J. Grune, Experiments on combustion regimes for hydrogen/air mixtures in a thin layer geometry, International Journal of Hydrogen Energy 44 (17) (2019) 8727–8742. doi:https://doi.org/10.1016/j.ijhydene.2018.11.144.
[18] Y. Han, M. Modestov, D. M. Valiev, Effect of momentum and heat losses on the hydrodynamic instability of a premixed equidiffusive flame in a hele–shaw cell, Physics of Fluids 33 (10) (2021) 103608. doi:https://doi.org/10.1063/5.0056707.
[19] F. Veiga-López, M. Kuznetsov, D. Martínez-Ruiz, E. Fernández-Tarrazo, J. Grune, M. Sánchez-Sanz, Unexpected propagation of ultra-lean hydrogen flames in narrow gaps, Physical review letters 124 (17) (2020) 174501. doi:https://doi.org/10.1103/PhysRevLett.124.174501.
[20] G. Gu, J. Huang, W. Han, C. Wang, Propagation of hydrogen–oxygen flames in hele-shaw cells, International Journal of Hydrogen Energy 46 (21) (2021) 12009–12015. doi:https://doi.org/10.1016/j.ijhydene.2021.01.071.
[21] P. Moskalev, V. Denisenko, I. Kirillov, Classification and dynamics of ultralean hydrogen–air flames in horizontal cylindrical hele–shaw cells, Journal of Experimental and Theoretical Physics 137 (1) (2023) 104–113. doi:https://doi.org/10.1134/S106377612307004X.
[22] B. Radisson, Dynamique non linéaire de fronts de flammes: expériences et modélisation, Ph.D. thesis, Aix-Marseille (2019).
URL https://www.theses.fr/2019AIXM0124
[23] A. Dejoan, C. Jiménez, V. N. Kurdyumov, Critical conditions for non-symmetric flame propagation in narrow channels: Influence of the flow rate, the thermal expansion, the lewis number and heat-losses, Combustion and Flame 209 (2019) 430–440. doi:https://doi.org/10.1016/j.combustflame.2019.08.011.
[24] C. Jiménez, D. Fernández-Galisteo, V. N. Kurdyumov, Flame-acoustics interaction for symmetric and non-symmetric flames propagating in a narrow duct from an open to a closed end, Combustion and Flame 225 (2021) 499–512. doi:https://doi.org/10.1016/j.combustflame.2020.11.026.
[25] B. Denet, Stationary solutions and neumann boundary conditions in the sivashinsky equation, Physical Review E 74 (3) (2006) 036303. doi:https://doi.org/10.1103/PhysRevE.74.036303.
[26] M. Matalon, The Darrieus–Landau instability of premixed flames, Fluid Dynamics Research 50 (5) (2018) 051412. doi:https://doi.org/10.1088/1873-7005/aab510.
[27] K. Bhairapurada, B. Denet, P. Boivin, A lattice-boltzmann study of premixed flames thermoacoustic instabilities, Combustion and Flame 240 (2022) 112049. doi:https://doi.org/10.1016/j.combustflame.2022.112049.
[28] C. E. Frouzakis, N. Fogla, A. G. Tomboulides, C. Altantzis, M. Matalon, Numerical study of unstable hydrogen/air flames: shape and propagation speed, Proceedings of the combustion institute 35 (1) (2015) 1087–1095. doi:https://doi.org/10.1016/j.proci.2014.05.132.
[29] L. Berger, K. Kleinheinz, A. Attili, H. Pitsch, Characteristic patterns of thermodiffusively unstable premixed lean hydrogen flames, Proceedings of the Combustion Institute 37 (2) (2019) 1879–1886. doi:https://doi.org/10.1016/j.proci.2018.06.072.
[30] Q. Michalski, C. J. B. Parejo, A. Claverie, J. Sotton, M. Bellenoue, An application of speckle-based background oriented schlieren for optical calorimetry, Experimental Thermal and Fluid Science 91 (2018) 470–478. doi:https://doi.org/10.1016/j.expthermflusci.2017.09.012.
[31] N. Otsu, A threshold selection method from gray-level histograms, IEEE Transactions on Systems, Man, and Cybernetics 9 (1) (1979) 62–66. doi:10.1109/TSMC.1979.4310076.

[32] M. Kuznetsov, S. Kobelt, J. Grune, T. Jordan, Flammability limits and laminar flame speed of hydrogen–air mixtures at sub-atmospheric pressures, International Journal of Hydrogen Energy 37 (22) (2012) 17580–17588, hySafe 1. doi:https://doi.org/10.1016/j.ijhydene.2012.05.049.
[33] Q. Liu, X. Chen, Y. Shen, Y. Zhang, Parameter extraction from spherically expanding flames propagated in hydrogen/air mixtures, International Journal of Hydrogen Energy 44 (2) (2019) 1227–1238. doi:https://doi.org/10.1016/j.ijhydene.2018.11.004.
[34] W. Kim, T. Namba, T. Johzaki, T. Endo, Self-similar propagation of spherically expanding flames in lean hydrogen–air mixtures, International Journal of Hydrogen Energy 45 (46) (2020) 25608–25614. doi:https://doi.org/10.1016/j.ijhydene.2020.06.261.
[35] B. C. Duva, E. Toulson, Unstretched unburned flame speed and burned gas Markstein length of diluted hydrogen/air mixtures, International Journal of Hydrogen Energy 47 (14) (2022) 9030–9044. doi:https://doi.org/10.1016/j.ijhydene.2021.12.217.
[36] G. Darrieus, Propagation d'un front de flamme, La Technique Moderne 30 (1938) 18.
[37] W. Kim, Y. Sato, T. Johzaki, T. Endo, D. Shimokuri, A. Miyoshi, Experimental study on self-acceleration in expanding spherical hydrogen-air flames, International Journal of Hydrogen Energy 43 (27) (2018) 12556–12564. doi:https://doi.org/10.1016/j.ijhydene.2018.04.153.
[38] C. Bauwens, J. M. Bergthorson, S. B. Dorofeev, Experimental investigation of spherical-flame acceleration in lean hydrogen-air mixtures, International Journal of Hydrogen Energy 42 (11) (2017) 7691–7697. doi:https://doi.org/10.1016/j.ijhydene.2016.05.028.
[39] W. Kim, T. Imamura, T. Mogi, R. Dobashi, Experimental investigation on the onset of cellular instabilities and acceleration of expanding spherical flames, International Journal of Hydrogen Energy 42 (21) (2017) 14821–14828. doi:https://doi.org/10.1016/j.ijhydene.2017.04.068.
[40] D. Fernández-Galisteo, A. Dejoan, J. Melguizo-Gavilanes, V. N. Kurdyumov, A three-dimensional study of the influence of momentum loss on hydrodynamically unstable premixed flames, Proceedings of the Combustion Institute (2022). doi:https://doi.org/10.1016/j.proci.2022.07.073.
[41] S. Shen, J. Wongwiwat, P. Ronney, Flame propagation in quasi-2D channels: stability, rates and scaling, in: AIAA Scitech 2019 Forum, 2019, p. 2365. doi:https://doi.org/10.2514/6.2019-2365.
[42] J. Bechtold, M. Matalon, The dependence of the Markstein length on stoichiometry, Combustion and flame 127 (1-2) (2001) 1906–1913. doi:https://doi.org/10.1016/S0010-2180(01)00297-8.
[43] F. Creta, P. E. Lapenna, R. Lamioni, N. Fogla, M. Matalon, Propagation of premixed flames in the presence of Darrieus–Landau and thermal diffusive instabilities, Combustion and Flame 216 (2020) 256–270. doi:https://doi.org/10.1016/j.combustflame.2020.02.030.
[44] L. Berger, A. Attili, H. Pitsch, Intrinsic instabilities in premixed hydrogen flames: parametric variation of pressure, equivalence ratio, and temperature. Part 2–Non-linear regime and flame speed enhancement, Combustion and Flame 240 (2022) 111936. doi:https://doi.org/10.1016/j.combustflame.2021.111936.
[45] F. Veiga-López, D. Martínez-Ruiz, M. Kuznetsov, M. Sánchez-Sanz, Thermoacoustic analysis of lean premixed hydrogen flames in narrow vertical channels, Fuel 278 (2020) 118212. doi:https://doi.org/10.1016/j.fuel.2020.118212.
[46] F. Foucher, S. Burnel, C. Mounaïm-Rousselle, M. Boukhalfa, B. Renou, M. Trinite, Flame wall interaction: effect of stretch, Experimental thermal and fluid science 27 (4) (2003) 431–437. doi:https://doi.org/10.1016/S0894-1777(02)00255-8.
[47] D. M. Michelson, G. I. Sivashinsky, Nonlinear analysis of hydrodynamic instability in laminar flames—II. numerical experiments, Acta astronautica 4 (11-12) (1977) 1207–1221. doi:https://doi.org/10.1016/0094-5765(77)90097-2.
[48] M. Matalon, C. Cui, J. Bechtold, Hydrodynamic theory of premixed flames: effects of stoichiometry, variable transport coefficients and arbitrary reaction orders, Journal of fluid mechanics 487 (2003) 179–210. doi:https://doi.org/10.1017/S0022112003004683.
[49] S. Kadowaki, The effects of heat loss on the burning velocity of cellular premixed flames generated by hydrodynamic and diffusive-thermal instabilities, Combustion and Flame 143 (3) (2005) 174–182. doi:https://doi.org/10.1016/j.combustflame.2005.05.012.

[50] D. G. Goodwin, H. K. Moffat, R. L. Speth, Cantera: An object-oriented software toolkit for chemical kinetics, thermodynamics, and transport processes, Caltech, Pasadena, CA (2009).
URL www.cantera.org

[51] R. Mével, S. Javoy, F. Lafosse, N. Chaumeix, G. Dupré, C. E. Paillard, Hydrogen-nitrous oxide delay time: shock tube experimental study and kinetic modelling, Proceedings of The Combustion Institute 32 (2009) 359–366. doi:https://doi.org/10.1016/j.proci.2008.06.171.

[52] R. Mével, S. Javoy, G. Dupré, A chemical kinetic study of the oxidation of silane by nitrous oxide, nitric oxide and oxygen, Proceedings of The Combustion Institute 33 (2011) 485–492. doi:https://doi.org/10.1016/j.proci.2010.05.076.

[53] S. Browne, J. Ziegler, J. Shepherd, Numerical solution methods for shock and detonation jump conditions, GALCIT report FM2006 6 (2008) 90.
URL https://shepherd.caltech.edu/EDL/PublicResources/sdt/

[54] J. Gaucherand, D. Laera, C. Schulze-Netzer, T. Poinsot, Intrinsic instabilities of hydrogen and hydrogen/ammonia premixed flames: Influence of equivalence ratio, fuel composition and pressure, Combustion and Flame 256 (2023) 112986. doi:https://doi.org/10.1016/j.combustflame.2023.112986.

[55] W. Han, P. Dai, X. Gou, Z. Chen, A review of laminar flame speeds of hydrogen and syngas measured from propagating spherical flames, Applications in Energy and Combustion Science 1-4 (2020) 100008. doi:https://doi.org/10.1016/j.jaecs.2020.100008.

[56] S. Bane, J. Ziegler, J. Shepherd, Development of one-step chemistry models for flame and ignition simulation, GALCIT Report GALTCITFM 2010 (2010) 53.
URL https://shepherd.caltech.edu/EDL/publications/reprints/galcit_fm2010-002.pdf

[57] S. H. Kang, S. W. Baek, H. G. Im, Effects of heat and momentum losses on the stability of premixed flames in a narrow channel, Combustion Theory and Modelling 10 (4) (2006) 659–681. doi:https://doi.org/10.1080/13647830600636049.

[58] J. Yanez, M. Kuznetsov, An analysis of flame instabilities for hydrogen–air mixtures based on sivashinsky equation, Physics Letters A 380 (33) (2016) 2549–2560. doi:https://doi.org/10.1016/j.physleta.2016.05.048.

[59] G. Bivol, A. Gavrikov, V. Golub, A. Elyanov, V. Volodin, 3D surface of an unstable hydrogen–air flame, Experimental Thermal and Fluid Science 121 (2021) 110265. doi:https://doi.org/10.1016/j.expthermflusci.2020.110265.

[60] J. Goulier, Comportements aux limites de flammes de prémélange hydrogène/air/diluants. étude de la transition flamme laminaire-flamme turbulente, Ph.D. thesis, Thesis, University of Orléans (2015).
URL https://www.irsn.fr/sites/default/files/documents/larecherche/formation_recherche/theses/theses-soutenues/dsr/2015-These_Goulier.pdf

[61] S. C. Taylor, Burning velocity and the influence of flame stretch, Ph.D. thesis, University of Leeds (1991).
URL https://etheses.whiterose.ac.uk/2099/1/SCTaylor.pdf

[62] N. Lamoureux, N. Djebaïli-Chaumeix, C.-E. Paillard, Laminar flame velocity determination for H2–air–He–CO2 mixtures using the spherical bomb method, Experimental Thermal and Fluid Science 27 (4) (2003) 385–393, second Mediterranean Combustion Symposium. doi:https://doi.org/10.1016/S0894-1777(02)00243-1.